Chemical Engineering Journal Advances 21 (2025) 100697

Contents lists available at ScienceDirect

Chemical Engineering Journal Advances

journal homepage: www.sciencedirect.com/journal/chemical-engineering-journal-advances

Producing hydrogen from biomass and seawater using immobilized carbon nitride photocatalysts

Ana L. Machado [a,b], Ricardo A. Oliveira [a,b], Goran Dražić [c], Joana C. Lopes [a,b], Cláudia G. Silva [a,b], Joaquim L. Faria [a,b], Maria J. Sampaio [a,b,*]

[a] LSRE-LCM – Laboratory of Separation and Reaction Engineering – Laboratory of Catalysis and Materials, Faculty of Engineering, University of Porto, Rua Dr. Roberto Frias, 4200-465 Porto, Portugal
[b] ALiCE – Associate Laboratory in Chemical Engineering, Faculty of Engineering, University of Porto, Rua Dr. Roberto Frias, 4200-465 Porto, Portugal
[c] Department of Materials Chemistry, National Institute of Chemistry, Hajdrihova 19, Ljubljana, Slovenia

ARTICLE INFO

Keywords:
Photocatalysis
Visible-light
Saccharides
3D-structure
H_2 evolution

ABSTRACT

To address the challenges related with using powdered catalysts and freshwater in photocatalytic hydrogen (H_2) production, this study explores the performance of carbon nitride-based catalyst immobilized on a 3D structure, employing seawater as a proton source. Methanol and saccharides such as cellobiose, fructose, glucose, saccharose and sorbitol were used as sacrificial agents to accelerate H_2 production via photoreforming. The results using immobilized photocatalyst showed that, at similar molar concentrations, glucose reveals higher efficiency compared with methanol, achieving an amount of H_2 evolution of 102 μmol after 180 min under visible light, compared to 45 μmol with methanol. Among the mono- and polysaccharides used, cellobiose has emerged as the most promising for H_2 evolution, achieving the highest amount of H_2 (124 μmol) after 180 min reaction. This result suggests a correlation between the efficiency of scavenging holes and the number of hydroxyl groups in the electron donor's structure. Despite a slight decrease in H_2 evolution compared with the powdered catalysts, the use of immobilized photocatalyst exhibited remarkable stability in both ultrapure water and seawater, maintaining its performance across multiple reuse cycles. The photocatalytic system demonstrated remarkable efficiency for H_2 production, avoiding phases separation processes, promotes the transition to continuous flow reactors and preserve freshwater resources.

1. Introduction

Due to the increasing energy demands, energy crisis, and environmental issues, the pursuit of sustainable and efficient energy sources has increased drastically. Among the various alternatives, hydrogen (H_2) has appeared as a promising candidate owing to its high energy content and the potential for clean combustion [1]. The photocatalytic reforming of biomass has gained significant attention as an attractive sustainable and cost-effective strategy for H_2 generation through the utilization of solar energy [2–8]. A great numerous of heterogenous photocatalysts, including metal oxides-based (e.g., TiO_2, ZnO, WO_3), metal-free catalysts such as carbon nitride-based materials and complex heterojunctions (*e.g.*, $CoWO_4/ZnIn_2S_4$ and $NiMoP_2$ modified with others semiconductors) have been explored for photocatalytic H_2 generation [3,6,7,9–13]. Most of the documented studies showed that the presence of co-catalysts is crucial to increasing the efficiency of the process for H_2 production by promoting electron-holes separation, hindering charge recombination, and enabling redox reaction at the photocatalysts surface. In the field of biomass reforming, the works published are mainly focused on the use of metal oxides-based photocatalysts and, more recently, on non-metal graphitic carbon nitride (g-C_3N_4) based materials, aiming to enhance the efficiency of the process in the visible spectral range. For example, A. Speltini et al. [14] reported the use of the commercial TiO_2 (Evonik AEROXIDE®) and a synthesized g-C_3N_4 coupled with Pt and Cu–Ni as cocatalysts for H_2 production by photocatalytic reforming of biomass under simulated solar light. The authors found that the organic g-C_3N_4 photocatalyst showed reasonable efficiency for H_2 production, however poor activity compared with the inorganic TiO_2-based photocatalyst. The authors pointed out the low specific surface area of the g-C_3N_4 (12.3 $m^2 g^{-1}$) compared with the 60.8 $m^2 g^{-1}$ of the commercial TiO_2. These findings have been showing that it is quite important to work on the design of efficient photocatalyst

* Corresponding author.
E-mail address: mjsampaio@fe.up.pt (M.J. Sampaio).

https://doi.org/10.1016/j.ceja.2024.100697

Available online 18 December 2024

systems, inhibiting the recombination between the photoexcited species (electrons and holes). Another study, reported by some of us [7] revealed the efficiency of carbon nanotubes-TiO_2 (CNT-TiO_2) composite materials for photocatalytic reforming of biomass (methanol and saccharides) using noble-metals (Pt, Pd, Au and Ir) as co-catalysts. Among the photocatalysts tested, Pt/(CNT-TiO_2)ox-473 exhibited the highest efficiency for H_2 evolution. The presence of CNT increased the specific surface area of the photocatalysts and the synergic effect between the metal and carbon phases, which was attributed to an enhancement in the efficiency of the charge carrier's separation and mobility. In the field of photocatalysis for H_2 production many of the reported studies focus on the development and improvement of the photocatalyst, aiming for wide H_2 yields [2–6,9,14–19]. Contrary, less attention has been directed towards the technological progress of supported photocatalysts, aiming eliminate separation steps, enable catalyst recovery and reusability, and overcome mass transfer limitations often faced with powdered materials. Various supports, including thin glass films, polymers, metal supports, and fibrous materials have been explored in different photocatalyst applications such as water/wastewater treatment, synthesis of highly valuable organic products and energy carriers [20–24]. An example is described by Xunliang Hu et al. [20], the authors studied the application of covalent triazine framework films as effective photocatalysts for H_2 generation. Although the authors revealed promising results using an immobilized catalyst, the Pt particles were added to the ethanol solution, therefore requiring its recovery at the end of the reactions.

The present study seeks to evaluate the efficiency of a g-C_3N_4-based catalyst for photocatalytic reforming of biomass for H_2 production under visible light irradiation. The efficiency of a photocatalyst consisting of g-C_3N_4 (GCNT) with a low fraction of platinum (0.6 wt.%) was explored in a slurry system using aqueous solutions of methanol and various saccharides as sacrificial agents (electron donors). The photocatalyst (here labeled as Pt/GCNT) was immobilized on a 3D-printed structure designed by manufacturing additive technique. The high stability of the 3D photocatalytic structure (Pt/GCNT-S) enabled an investigation, involving seawater as an alternative water source for H_2 generation from biomass derivatives, striving for the sustainability of the process.

2. Experimental

2.1. Chemical and materials

Dicyandiamide (DCN, 99 %), poly(vinylidene fluoride) (PVDF), N-methyl-2-pyrrolidone (NMP, 99,5 %), polyvinylpyrrolidone (PVP), and perfluorinated resin solution (Nafion™) were acquired from Sigma–Aldrich. Glucose anhydrous (GLU, 98 %), sorbitol (SOR, 99 %), and dihydrogen hexachloroplatinate (IV) hexahydrate ($H_2PtCl_6{\cdot}_6H_2O$) were purchased from Alfa Aesar. Fructose (FRT, 99 %), cellobiose (CLB, 98 %) and saccharose (SCR, 98 %) were acquired from Acros Organics. Methanol (MeOH, $\geq$ 99.9 %) was supplied from Fluka. Ethanol absolute ($\geq$ 99.8 %), sulfuric acid (95 %) and nitric acid (65 %) were obtained from VWR. Ultrapure (UP) water, with a resistivity of 18.2 MΩ cm at 25 °C, was produced using a Milli-Q water system. Seawater was collected in Foz do Douro, Northern Portugal and used without prior treatments (Table S1).

2.2. Synthesis and immobilization of the photocatalyst

To prepare the bulk carbon nitride (GCN), a specific amount of DCN was thermally decomposed at 550 °C under a static air atmosphere using a Phoenix Microwave Muffle Furnace (CEM Corporation) [21,22]. A second thermal treatment was conducted on the bulk material at 500 °C for 2 h (SD, Scheme S1) to obtain the thermally exfoliated material (GCNT). As a result of this post-treatment, the specific surface area of the photocatalyst increased approximately 15-fold, from 7 to 105 ± 5 $m^2 g^{-1}$ [21,22].

The incipient wetness impregnation method was employed for loading the metal phase (Pt) onto the catalyst using the corresponding metal salt solution [25]. The sample was dried at 100 °C, following the thermal treatment under a nitrogen flow (50 ml L^{-1}) for 1 h and subsequently reduced under hydrogen flow (50 ml L^{-1}) for 3 h at 200 °C. Although the theoretical metal content was set at 1 wt.%, from inductively coupled plasma optical emission spectroscopy (ICP-OES), it was found that the value of Pt0 loaded on the photocatalyst was 0.60 wt.%.

The Pt/GCNT powdered photocatalyst was immobilized on a 3D-printed structure with an external area of 88 cm^2 previously coated with a poly(vinylidene fluoride) – PVDF solution film, which acts as an adherent agent for the photocatalyst [21,22]. Briefly, a thin layer PVDF was spread on the polylactic acid (PLA) 3D structure followed by the dispersion of the Pt/GCNT photocatalyst (with an average of ca. 120 mg of the powder catalyst dispersed on the external surface of the 3D structure; SD, Scheme S1). The Pt/GCNT-S photocatalyst was rapidly immersed in distilled water, allowing the liquid/solid phase inversion of the polymer.

2.3. Photocatalyst characterization

The Brunauer–Emmett–Teller (BET) method was used to calculate the specific surface area (S_{BET}) of the powdered samples based on N_2 adsorption-desorption isotherms acquired at −196 °C.

The content of platinum on the GCNT was determined by Inductively Coupled Plasma Optical Emission Spectrometry (ICP-OES) using an ICAP 7400 THERMO apparatus (Massachusetts, United States) equipped with a nebulizing system and optical emission spectroscopy for detection. Briefly, 25 mg of Pt/GCNT sample was dispersed in 10 mL of HNO_3 (65 %), the temperature was raised to 140 °C and remained for 2 h Then, the acidic solution was diluted and subjected to chemical analysis. The measurements were conducted in triplicate, and the mean value was considered as the result.

The morphology of the photocatalysts was examined by scanning electron microscopy (SEM) using a FEI Quanta 400 FEG ESEM/EDAX Genesis X4M (15 keV) instrument. Certain images were acquired using a Phenom ProX device to confirm the stability of the morphology exhibited by the supported materials.

The photocatalysts were examined by conventional and high-resolution transmission electron microscopy (TEM/HRTEM). Additionally, atomically resolved scanning transmission electron microscopy (STEM) measurements were also performed using a Cs probe-corrected TEM/STEM Jeol ARM 200 CF microscope equipped with a cold-FEG electron source. To minimize the electron-beam induced damages 80 kV accelerating voltage was used

The optical absorption of the photocatalysts (powder and immobilized) was monitored by diffuse reflectance UV–Vis (DRUV–Vis) spectroscopy using a JASCO V-560 spectrophotometer equipped with an integrating sphere.

Photoluminescence (PL) analysis of the photocatalysts was conducted at room temperature on a JASCO (FP 82000) fluorescence spectrometer with a 150 W Xenon lamp as light source, using bandwidths of 2.5 nm for both emission and excitation.

The photoelectrochemical measurements were carried out using a ZAHNER ZENNIUM pro electrochemical workstation (ZAHNER-Elektrik, Germany) coupled with a PP-211 external potentiostat and a ZAHNER CIMPS system. A three-electrode cell arrangement was used, including a working electrode, a counter electrode (Pt wire) and a reference electrode (Ag/AgCl, 1 N KCl). The working electrodes were supported by fluorine-doped tin oxide-coated glass (FTO glass). The photocatalyst (5 mg), 5 wt % Nafion solution (50 μL) and EtOH (1 mL) were stirred overnight. The resulting slurry was spread on FTO glass and heated for 30 min at 150 °C. The electrolyte was an H_2SO_4 aqueous solution (1 M). The transient photocurrent (TPC) response was evaluated using a high-intensity visible light emitted diode (LED) throughout 110 s with periods of 10 s light-on and 10 s light-off. The electrochemical

impedance spectroscopy (EIS) measurements were carried out between 100 kHz and 100 mHz, applying a potential range of 0.6 V vs Ag/AgCl. The Mott-Schottky plots were generated using the ThalesXT software within the same potential range as the cyclic voltammograms (CV), which were acquired by scanning the potential from 1.5 to 1.5 V versus Ag/AgCl at a scan rate of 10 mV s^{-1}.

2.4. Photocatalytic reaction setup

To evaluate the photocatalytic H_2 production, a borosilicate reactor glass was filled with 100 mL of aqueous solutions of sacrificial species, such as methanol (MeOH) or saccharides (cellobiose "CLB", fructose "FRT", glucose "GLU", saccharose "SCR" and sorbitol "SOR"). The initial concentration of these solutions was set at 2.5 M or 0.02 M, depending on their nature and solubility. The reactions were carried out at constant temperature (~20 °C) and at natural pH (6.4 and 7.8 for ultrapure water "UP" and seawater "SW", respectively). The LED system used comprises four visible LEDs (λ_{max} = 417 nm with an average light intensity (*I*) of 109 mW cm^{-2} at 3 cm from the external reactor wall, and 74 mW cm^{-2} at 4 cm from the refrigeration system, where the immobilized Pt/GCNT-S photocatalyst was fixed (Scheme 1).

Prior to starting the photocatalytic reactions, the reactor was sealed, and the solutions were degassed under nitrogen flow for 30 min to remove the dissolved oxygen. Then, the N_2 flow was fixed at 7.5 mL min^{-1} and the LED system was switched on. An Inficon Micro GC 3000 gas chromatograph analyzer, equipped with a molsieve column and a micro-TCD detector was employed for assessing the H_2 production using argon as the carrier gas. When Pt/GCNT photocatalyst was used in slurry reactions, the catalyst load was fixed at 1.0 g L^{-1}. In experiments using seawater (SW) as a proton source, a similar experimental procedure was performed. Selected photocatalytic experiments were conducted in triplicate with the standard deviation remaining below 4 %.

3. Results and discussion

3.1. Photocatalyst characterization

The comprehensive characterization analyses of the GCN bulk and GCNT powdered samples employed in this study have been comprehensively addressed in our prior publications [21,22]. Hence, the techniques here described are mostly directed toward the platinum-containing material (Pt/GCNT), both in its powdered state and its immobilization on the PLA structure. Nevertheless, for sake of clarity, the morphology of the powdered photocatalysts is displayed in Fig. S1 (SD). The SEM images revealed the characteristic morphology of carbon nitride materials of bulk GCN, *i.e.*, a compact stacked lamellar structure is noticed (Fig. S1a). After the bulk material suffered thermal exfoliation, the resulting material (GCNT) presented thin layers and particle aggregates, which led to a higher specific surface area (105 ± 5 $m^2 g^{-1}$) compared with 7 $m^2 g^{-1}$ obtained for the bulk material. After Pt load, the resulting photocatalyst (Pt/GCNT) shows similar morphology (Fig. S1c), which corroborates with the results obtained from S_{BET} analysis, *i.e.*, negligible changes were noticed (101 ± 5 $m^2 g^{-1}$). Although some studies report an increase on the S_{BET} when noble metals are loaded in the photocatalyst surface due to possible changes in their textural properties, in the present study this value remained unchanged. This seems to be ascribed to the mild thermal treatment applied to the Pt/GCNT material (200 °C, N_2 and H_2), leading to negligible modifications of the textural and morphological properties of the material.

SEM measurements were assessed to examine the morphology of neat PLA structure as well as coated with a thin film of PVDF polymeric solution (Fig. 1a and b, respectively).

Fig. 1a illustrates the typical PLA layers resulted from the additive manufacturing process. Upon coating the surface of the PLA structure with the PVDF, the structure reveals a regular morphology with the usual small pores of this polymer (Fig. 1b) [26]. As shown in Fig. 1c, the Pt/GCNT immobilized on the 3D structure maintained its morphology (as revealed in Fig. S1), which was expected since the coating only involved a simple deposition of the powdered photocatalyst on the thin film of the PVDF prior the final polymerization process. Analyzing the cross-section of the Pt/GCNT-S structure, it can be observed the three constituents' phases, *i.e.*, the PLA, the PVDF and the photocatalyst (Fig. 1d, e and f).

The optical and electronic properties of the Pt/GCNT-S structure were investigated by DRUV–Vis and PL spectroscopies (Fig. S2, SD) and compared with those of the powdered materials. As previously documented [21,22], the DRUV–Vis analysis shows that GCNT presents a broad band fading ca. 450 nm, indicating its capacity to absorb visible light. When Pt particles were loaded (Pt/GCNT), a slight increase in the absorption band was noticed throughout the visible range, which is commonly attributed to the localize surface plasmon resonance of noble metals. Additionally, from the DRUV–Vis spectra (Fig. S2a, SD) was obtained the *Tauc* plot (Fig. S2b, SD). This analysis revealed that the presence of Pt nanoparticles on GCNT led to a negligible decrease in the bandgap energy, from 2.76 eV for GCNT to 2.70 eV for Pt/GCNT.

The microstructure of GCNT-based materials was investigated by HAADF-STEM (Fig. 2). Both neat GCNT and Pt/GCNT exhibited an amorphous structure with a slate-like and 2D lamellar assembly with various mesopores being observed (Fig. 2a and b). This characteristic may indicate a high surface area, promoting the exposure of a great number of reactive active sites at the photocatalyst surface, which corroborates with SEM and S_{BET} analyses. Moreover, HAADF-STEM micrographs at higher showed high homogeneity of the atomic dispersion of crystalline Pt nanoparticles with a diameter of ca. 3.0 nm with a

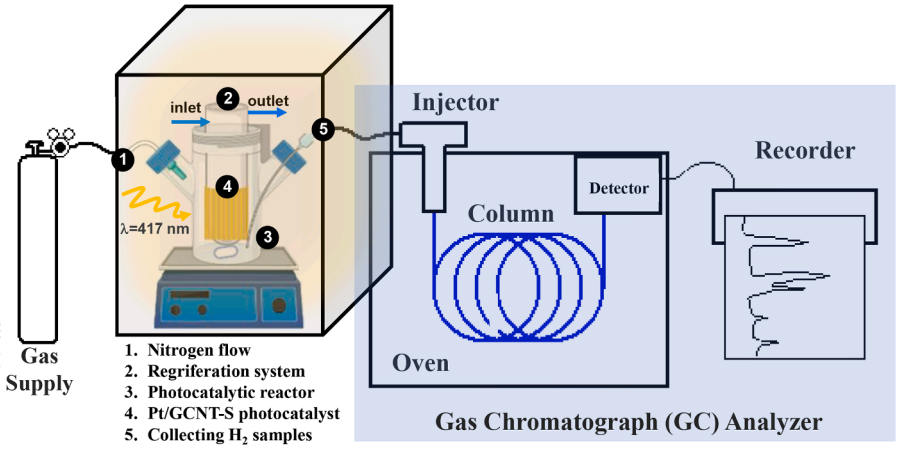

Scheme 1. Scheme of the photocatalytic setup for hydrogen production.

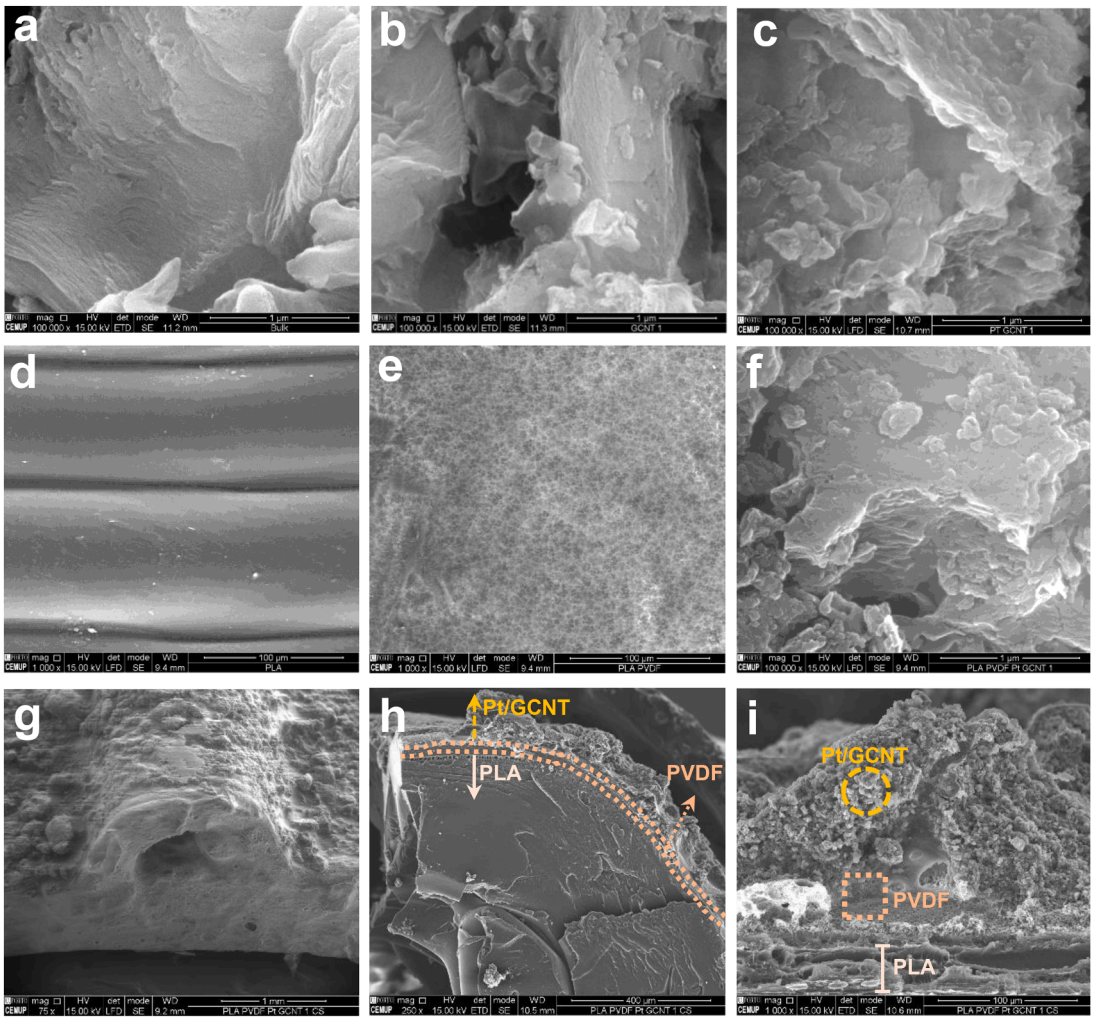

Fig. 1. SEM images of neat PLA 3D structure (a), PLA 3D structure coated with PVDF (b), Pt/GCNT-S photocatalyst front view (c) and cross section (d, e and f).

standard deviation of 1.2 nm on the GCNT layers (Fig. 2 b_3), which was confirmed by analysis of size distribution measured with ImageJ software, as shown in Fig. S3. While this analysis allowed us to confirm that Pt nanoparticles are mostly in the form of single atoms, some sparse superfine nanoclusters with a diameter at the subnanometer scale are also noticeable (Fig. 2 b_6). To further investigate the elemental distribution of the metal phase on the GCNT, mapping of N, C and Pt elements was carried out by EDXS as shown in Fig. 2c. The well-defined maps of N, C, and Pt exhibited sharp contrast, demonstrating that these elements were uniformly distributed throughout the entire composite material, which provides solid evidence of the successful loading of Pt nanoparticles on the photocatalyst.

Concerning the results obtained from PL measurements (Fig. S2c, SD), the wide quenching of luminescence observed when Pt particles were added to the GCNT photocatalysts, suggesting that the noble metal acts as an active scavenger of photogenerated electrons generated at the GCNT surface under visible light. These results corroborate with results obtained from electrochemical analyses (Fig. 3). The photocurrent response characteristics of the prepared photocatalysts were evaluated under visible LED irradiation. Pt/GCNT exhibited slightly higher photocurrent density than GCNT, suggesting that the doping effect of Pt atoms on GCNT can facilitate the interfacial separation and transfer of photoinduced electron.hole pairs. These results were further confirmed by electrochemical impedance spectroscopy (EIS) studies shown in Fig. 3b. As observed, Pt/GCNT shows the smallest partial arc in the Nyquist plot compared to neat GCNT (open symbols), indicating improved charge transfer properties. Additionally, EIS curves were simulated using an equivalent circuit diagram. The results from the simulated Nyquist plot (filled symbols) show large semicircles radius and high impedance values, suggesting high charge-transfer resistance at the electrode interface. This could be related to poor electrode interface properties since the immobilization of GCNT-based materials onto the FTO surface can be challenging. Consequently, the electrodes might become damaged during the experiments, resulting in increased resistance.

To further explore the photocatalytic performance for H_2 production, the Mott–Schottky electrochemical assessment was used to determine the flat band potential (V_{FB}) of the photocatalysts (Fig. 3c). These values were obtained by the linear interception with the potential axis at different frequencies [27]. As displayed in Fig. 3c, GCNT and Pt/GCNT revealed a typical n-type semiconductor characteristic, i.e., indicates that the majority carriers in the optical semiconductor are electrons, as the Mott-Schottky plots show positive slopes. The V_{FB} for neat GCNT and Pt/GCNT were determined as −0.92 V and −0.87 V, respectively. In addition, the conduction band potential (V_{CB}) was calculated concerning the normal hydrogen electrode (NHE) at pH 7, following the equation $V_{CB} = V_{FB}\left(\frac{Ag}{AgCl}, pH\right) + \Delta V\left(\frac{Ag}{AgCl}, pH\right) - 0.059(7 - pH)$, where $\Delta V\left(\frac{Ag}{AgCl}, pH\right)$ is the Ag/AgCl potential against NHE (0.21 V). The CB potential of each material was calculated by combining the formula

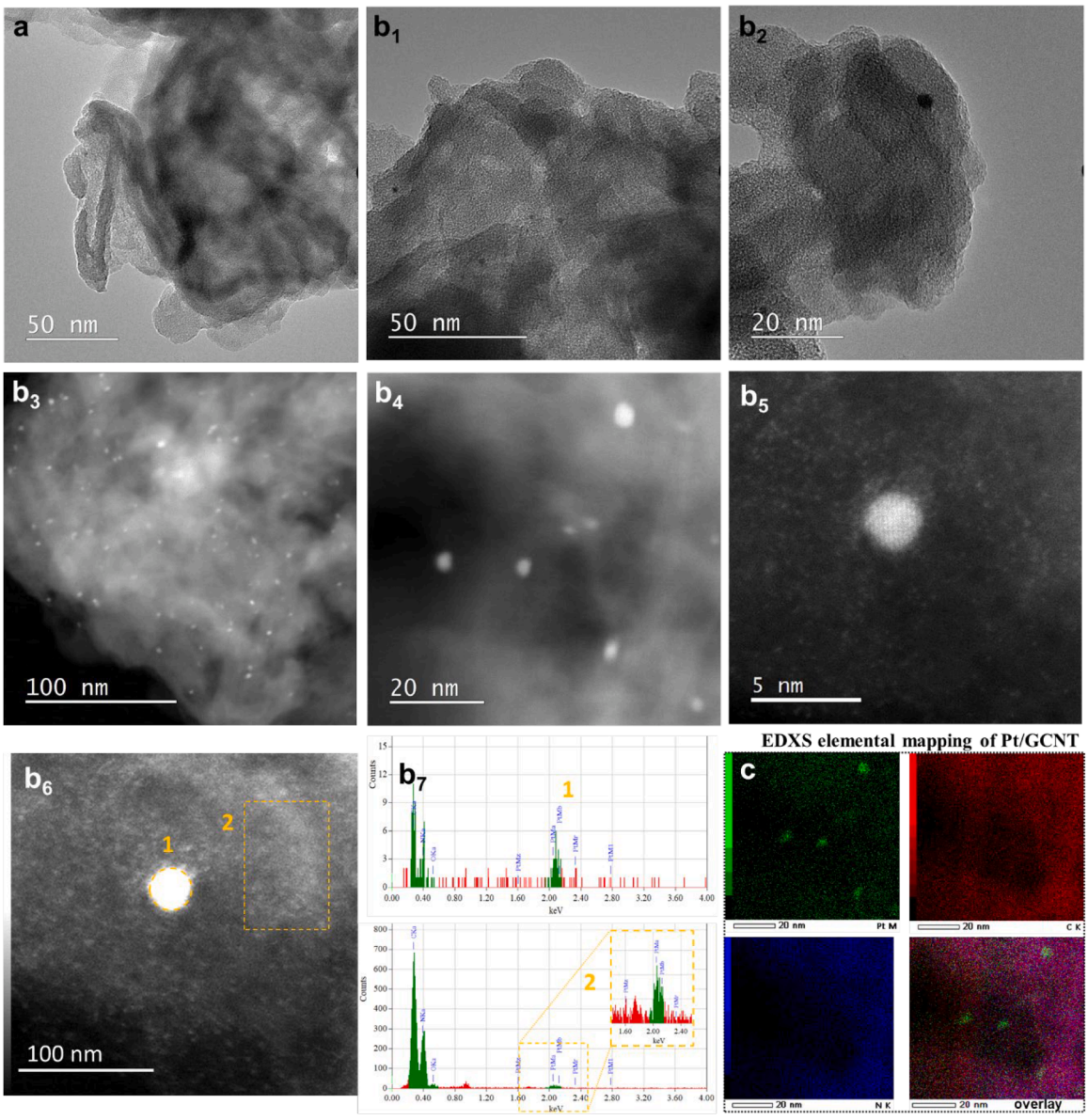

Fig. 2. TEM images of neat GCNT (a) and Pt/GCNT (b) – the numeration 1–6 corresponds to a different magnification of Pt/GCNT and b_7 show the EDXS spectra of respective zones indicated in b6 for Pt nanoparticle (1) and Pt single atoms (2). EDXS mapping of the Pt/GCNT photocatalyst (c).

$V_{CB} = V_{VB} - \frac{E_g}{e}$ with the bandgap energy (E_g) derived from the *Tauc* plot (Fig. S2b, SD). The V_{CB} of neat GCNT and Pt/GCNT noticed were −0.98 and −0.93 V *vs.* NHE, respectively.

These observations suggest that both photocatalysts show similar energy levels, which may indicate that the presence of Pt nanoparticles negligible affects the electronic properties of the GCNT. Nevertheless, even a small load (0.6 %) of Pt nanoparticles can introduce catalytic properties such as increased electron mobility. In addition, Pt nanoparticles serve as active sites for H_2 evolution, enhancing the efficiency of the material, despite the electronic structure of the based material being unchanged.

Cyclic voltammetry (CV) was employed to assess the charge transfer capabilities of the prepared materials. As depicted in Fig. 3d, Pt/GCNT exhibits superior current density in both reduction and oxidation peaks, indicating excellent electrochemical properties. In addition, this suggests improved charge separation and enhance electron accumulation at the photocatalyst surface [28], which corroborates the results obtained by photocurrent, EIS and PL analyses. These findings, combined with the negligible differences in bandgap energies between the photocatalysts (GCNT and Pt/GCNT), suggest that the presence of Pt nanoparticles and single Pt atoms can significantly enhance charge separation. This is achieved by the efficient trapping of electrons from the CB of GCNT by Pt particles, which act as highly effective active sites for proton reduction. In addition, the presence of sacrificial agents, such as biomass derivatives, can significantly contribute to H_2 production. The oxidation of these organic compounds generates additional electrons, thereby lowering the kinetic barriers typically associated with water oxidation (Fig. 4).

3.2. Photocatalytic hydrogen evolution

Due to the favorable features of MeOH such as high H:C ratio, simple molecule structure and its potential as derivative from biomass sources, this chemical is commonly used as sacrificial agent (electron donor) in the photocatalytic reforming for H_2 production [7,29]. Yet, the use of MeOH may pose significant concerns in the field of photocatalytic reforming, due to its toxicity both to humans and the environment, especially if release or leakage occurs during the process, as well as the

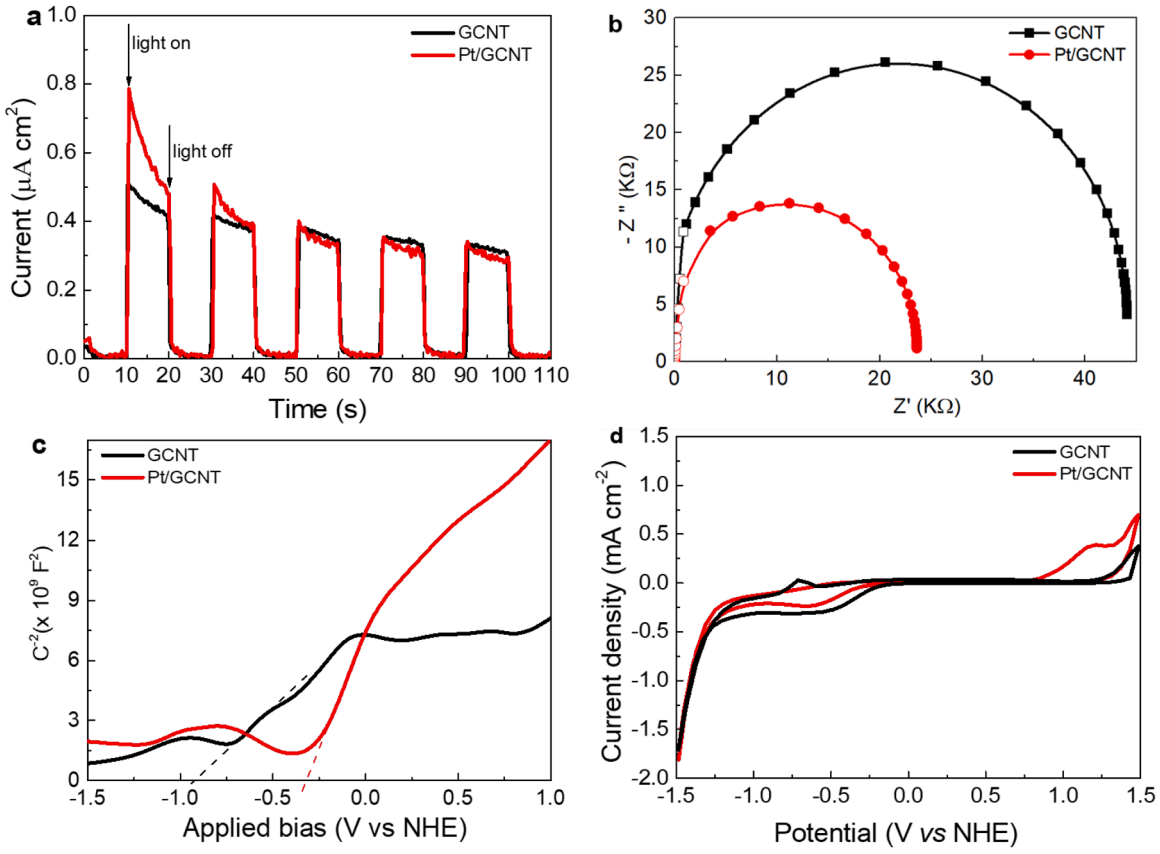

Fig. 3. (a) Transient photocurrent, (b) electrochemical impedance, (c) Mott–Schottky plots, and (d) cyclic voltammograms for GCNT and Pt/GCNT materials.

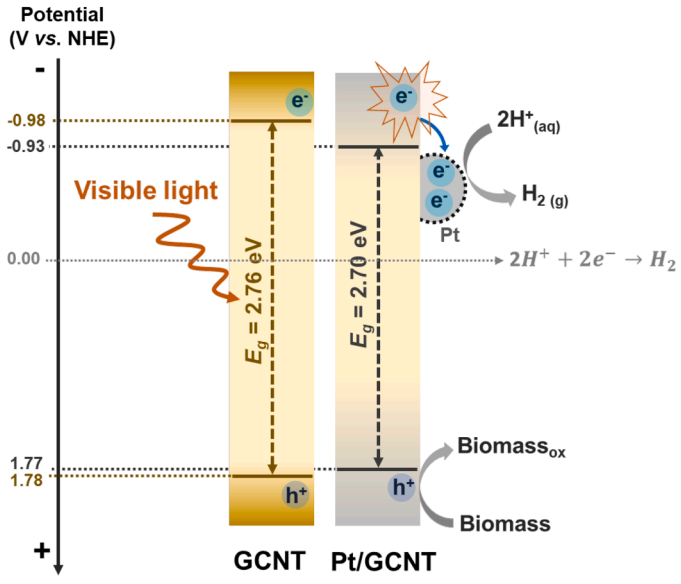

Fig. 4. Simplified band structure of GCNT and Pt/GCNT photocatalysts.

generation of some noxious by-products (*e.g.*, formaldehyde). Thus, some efforts have been explored to find sustainable and non-toxic alternative feedstocks to replace MeOH in the field of H_2 photocatalytic reforming. Instead, saccharides resulting from biomass sources can offer a viable solution that aligns with the principles of green chemistry [6–8,29].

Here, the photocatalytic H_2 generation was first carried out to investigate the influence of sacrificial agent (SA) using MeOH at different initial concentration levels (2.5 M and 0.02 M) and its comparison with glucose (GLU) was examined at low concentrations. As displayed in Fig. 5a, using the Pt/GCNT photocatalyst suspensions, the H_2 generation follows the order 2.5 M MeOH > 0.02 M GLU > 0.02 M MeOH, being obtained of 470 μmol, 133 μmol and 50 μmol of H_2 after 120 min reaction, respectively. In the absence of SA, no production of H_2 was observed. The abrupt decrease of the initial concentration of SA from 2.5 M to 0.02 M (>100-fold) was due to the limited solubility of GLU in water, otherwise, it would be quite difficult to compare the results. These experiments showed that at similar initial concentrations (0.02 M), GLU is an alternative electron donor of MeOH in the photocatalytic reforming for H_2 evolution. The main advantage of using GLU is the possibility of its obtention from biomass derivatives through processes such as hydrolysis or fermentation of organic matter from plants and animals [30].

Concerning the results obtained using the immobilized Pt/GCNT-S photocatalyst, similar tendency was observed for H_2 production: 2.5 M MeOH > 0.02 M GLU > 0.02 M MeOH, *i.e.*, 314 μmol, 102 μmol and 45 μmol after 180 min of reaction (Fig. 5b). Nevertheless, lower efficiency for H_2 generation, using immobilized Pt/GCNT-S was noticed, which seems to be ascribed to the lower photocatalyst-solution interface compared with the slurry reactions. SEM images of the Pt/GCNT-S structure showed that the photocatalyst did not cover the entire structure, leaving some areas where the PVDF film (non-reactive area) was the component exposed to both light and subtract (Fig. 1e and f). Additionally, it is important to note that the light intensity reaching the surface of the photocatalyst structure is lower (74 mW cm^{-2}) compared to that in the slurry systems (109 mW cm^{-2}), *i.e.*, fewer photons are achieving the reactive sites of the catalyst. Although the Pt/GCNT-S structure revealed less performance, from the technological point of view, the immobilization of the catalysts offers significant advantages, including improved light absorption, enhanced photocatalyst stability,

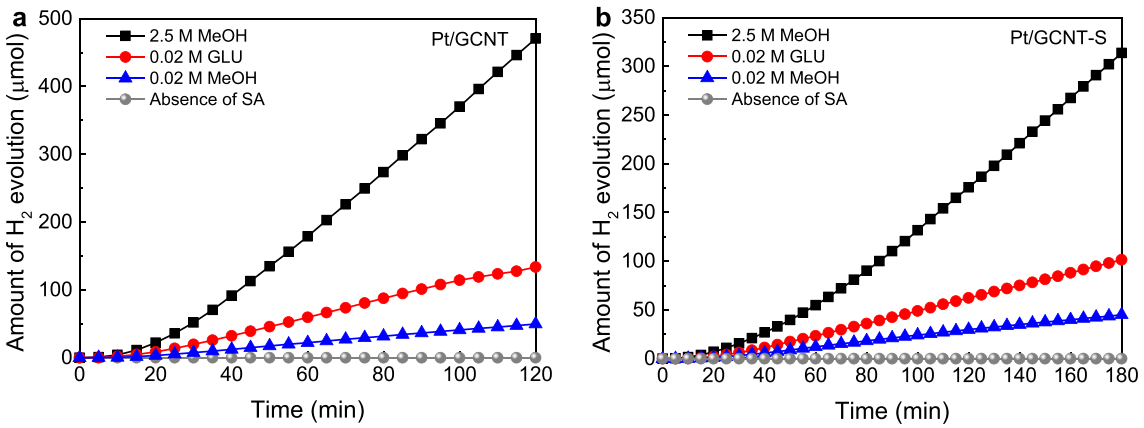

Fig. 5. (a) H_2 evolution using Pt/GCNT suspensions and (b and c) immobilized Pt/GCNT-S in ultrapure water in the absence of SA and with different initial concentrations of SA. Experimental conditions: 100 mL UP solutions containing $[MeOH]_0 = 2.5$ M or 0.02 M, [GLU] = 0.02 M; catalyst load fixed at 1.0 g L^{-1} (slurry) and 88 cm^2 of photoactive area (immobilized Pt/GCNT-S); and irradiation source ($\lambda_{exc} = 417$ nm; $I = 74$ or 109 mW cm^{-2}, immobilized and slurry, respectively).

simplified and low-cost separation processes and promote scalability for continuous systems. These findings emphasize that the characteristics of the photocatalysts are crucial for specific applications such as H_2 generation. It is also important to consider all the operational parameters involved in the process if the main goal is the practical application. These parameters include the immobilization of the catalysts, aiming to avoid separation process costs, the stability and reusability of the photocatalyst. Thus, to overcome and understand some of these barriers, the evolution of H_2 was investigated using the immobilized photocatalyst under the most extreme experimental conditions, *i.e.*, using the highest concentration of MeOH as an electron donor. Before each run, the Pt/GCNT-S immobilized structure was thoroughly washed with water under sonication for 3 min, followed by drying at ca. 40 °C for 4 h. It is also important to emphasize that the same immobilized photocatalyst structure (Pt/GCNT-S) was employed in all reactions presented in this study (>120 h of use), which indicates its stability under the reaction conditions.

As shown in Fig. S4 (SD), the immobilized Pt/GCNT-S photocatalyst maintains its activity for three cycles, suggesting good stability under the reaction conditions employed (UP water SA solutions). In addition, a

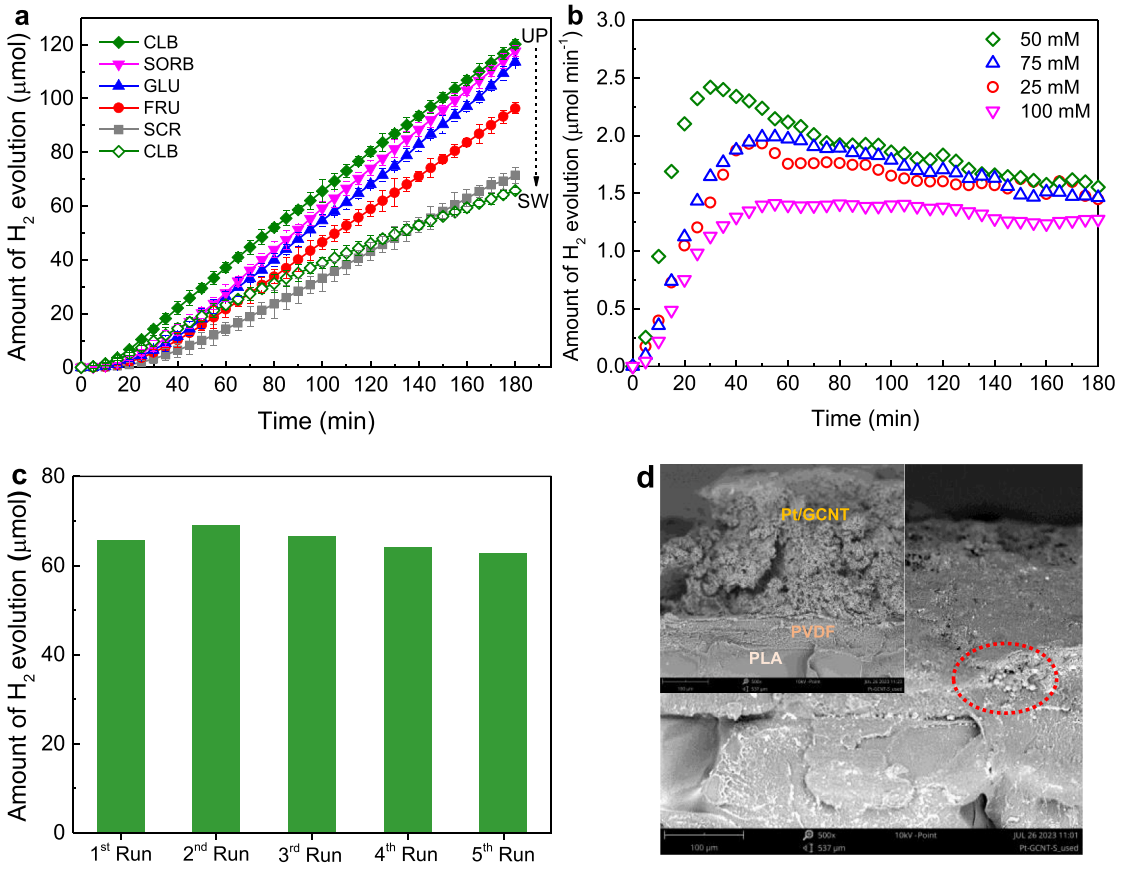

Fig. 6. (a) Screening of various SA for H_2 evolution using immobilized Pt/GCNT-S in ultrapure water (filled symbols) and SW (open symbols). (b) Effect of initial concentration of CLB and (c) reusability assessment of Pt/GCNT-S using SW as water matrix. Experimental conditions: 100 mL of SA solutions (25–100 mM); 88 cm^2 of photoactive area (immobilized Pt/GCNT-S); and irradiation source ($\lambda_{exc} = 417$ nm; $I = 74$ mW cm^{-2}).

slight increase in H_2 evolution from the first to second and third runs was noticed, which can be ascribed to certain fluctuations of the operational parameters or partial photoreduction of oxidized Pt species (co-catalyst) during the H_2 evolution reaction under visible light excitation. Indeed, some studies report the use of light-induced methods to reduce Pt^{4+} ions to Pt^0 nanoparticles, seeking to increase their activity and stability [31, 32]. Concerning the required presence of SA, studies have documented the use of biomass derivatives such as saccharides on photocatalytic reforming for H_2 evolution, aiming for the sustainability of the process. For instance, in our previous work was evaluated the capability of TiO_2 and CNT-TiO_2 based catalysts in the presence of metals as cocatalyst (Pt, Pd, Au and Ir) for photocatalytic reforming of saccharides (arabinose, glucose, fructose and cellobiose) under near UV–Visible light [7].

Although, in the present study, better efficiency for H_2 generation was attained using MeOH as an electron donor at extremely high concentrations, the study was followed with a lower concentration of SA of selected saccharides to explore their potential for H_2 production using the developed immobilized Pt/GCNT-S photocatalyst. In these experiments, we increased and maintained the initial molar concentration of the saccharides to 0.05 M based on our findings from the previous work that demonstrated higher concentrations of SA enhance the scavenging efficiency of the generated holes [21]. Among the mono- and polysaccharides, used as electron donors, CLB revealed the highest efficiency for H_2 production, followed by SORB > GLU > FRU > SCR (Fig. 6a), suggesting that molecules with a high number of –OH groups present in the molecule skeleton are the main responsible for the photocatalytic H_2 production. Indeed, this observation aligns with findings from our previous research on H_2O_2 production, which also employed neat GCNT as the photocatalyst [21]. The superior amount of H_2 evolution seems to be explained by the great number of –OH groups on the molecular structure of the polyhydroxy compounds, by the higher effective molarity, and by the faster diffusion of CLB in water [21,33,34].

As previously mentioned, it is quite important to avoid the use of freshwater to produce any class of energy carriers. Some studies have been performed in the field of H_2 photocatalytic evolution to implement sustainable solutions and to find alternative water sources, such as seawater and wastewater [35,36], seeking to mitigate the utilization of surface water or other freshwater supplies. In this sense, the study was followed using seawater (SW) as water source. As displayed in Fig. 6a, when SW was employed, the amount of H_2 evolution decreased by around 50 % using CLB as an electron donor. To evaluate the effect of CLB on the photoreforming for H_2 production, the initial concentration was examined at 25–100 mM using SW as a water source (Fig. 6b). Experiments were not conducted with concentrations above 100 mM since this already constitutes approximately one-third of CLB's solubility in water (12 g per 100 mL at 25 °C (equivalent to 351 mM)).

Under these conditions, the maximum amount of H_2 produced was 2.42 μmol min^{-1} using 50 mM of CLB. Increasing the SA initial concentration led to a decrease in H_2 production, suggesting that all the catalytic sites are occupied, and the reaction rate becomes independent of SA concentration. This study achieved the comparable amount of H_2 generation by using an immobilized catalyst under visible light, compared to our previous work, which used a powdered Pt/TiO_2–473 catalyst under near UV–visible light with 20 mM of CLB as a SA [7]. Experiments in the absence of SA were also conducted but no production of H_2 was noticed, which highlights the crucial role of effective SA in the photocatalytic process.

Moreover, the decrease in H_2 production when SW was employed compared with UP water was already expected. SW contains a variety of salts, organic and inorganic compounds and biological species that can interfere with the photocatalytic performance, stability, and durability of the catalysts. The commonly high salinity can lead to active site blockage and catalyst deactivation. In addition, during the photocatalytic process, it is possible to release some toxic byproducts, such as chlorine gas, hypochlorous acid, and other chlorinated compounds, which can be toxic to both environment and humans [37]. Nevertheless, despite the challenges, the use of SW can significantly contribute to sustainable H_2 production, especially in regions where freshwater is scarce. Thus, it is quite needed to find solutions to address these issues, such as developing robust catalysts, implementing effective pre-treatment methods to remove the most damaging compounds from SW and optimize the photocatalytic reaction system. From the preliminary studies performed using SW was found that under the reaction conditions, the photocatalytic structure remained stable at least for 5 cycles (Fig. 6c). Although the performance remained significatively stable, analyzing the morphology of the Pt/GCNT-S structure after these cycles were observed which seemed to be micro-organisms (non-fermenting gram-negative rods, Fig. 6d) [38], suggesting the possibility of biofouling occurrence.

As previously mentioned, between each run, the immobilized photocatalyst was continuously washed, which increases the costs in real applications. Nevertheless, this study emphasizes the importance of transition towards renewable energy systems with further research and development to enhance the applicability of the photocatalytic systems in real scenarios.

4. Conclusions

This study demonstrated the potential of Pt/GCNT photocatalysts for H_2 production through photocatalytic reforming of saccharides under visible light exposure. Despite the costs associated with the use of Pt nanoparticles, its role as a cocatalyst was required to facilitate the conversion of protons and electrons into H_2 by working in tandem with the GCNT photocatalyst. While a higher concentration of MeOH (2.5 M) led to enhanced amounts of H_2 production, the use of saccharides at low concentrations (0.02 M) are a greener alternative and generated significant amounts of H_2 compared with similar concentrations of MeOH. Among the saccharides tested, 0.05 M of cellobiose revealed the highest amount of H_2 production. The results showed that the scavenging efficiency of photogenerated holes quickly rises with the number of –OH groups in the molecular skeleton of the saccharides. The stability and reusability of Pt/GCNT-S were confirmed using both water matrices (UP and SW), with minimal loss in its activity over several cycles. Although the photocatalytic activity of Pt/GCNT-S was lower in seawater, due to its complex composition, the results provide insights for further exploration of photocatalytic systems using seawater as a water resource for H_2 production.

Funding

This work was supported by national funds through FCT/MCTES (PIDDAC): LSRE-LCM, UIDB/50020/2020 (DOI: 10.54499/UIDP/50020/2020) and UIDP/50020/2020 (DOI: 10.54499/UIDP/50020/2020); ALiCE, LA/P/0045/2020 (DOI: 10.54499/LA/P/0045/2020) and 2022.04682.PTDC (SuN2Fuel). M.J.S. acknowledges FCT funding under the Scientific Employment Stimulus - Institutional Call CEECINST/00010/2021/CP1770/CT0011 (10.54499/CEECINST/00010/2021/CP1770/CT0011). A.L.M. thanks her scholarship to the Fundação Calouste Gulbenkian. JCL acknowledges the PhD research grant from FCT, Ref. 2020.04651.BD (DOI: 10.54499/2020.04651.BD).

CRediT authorship contribution statement

Ana L. Machado: Writing – original draft, Investigation, Data curation. **Ricardo A. Oliveira:** Investigation, Data curation. **Goran Dražić:** Writing – review & editing, Investigation, Formal analysis, Data curation. **Joana C. Lopes:** Writing – review & editing, Investigation, Data curation. **Cláudia G. Silva:** Writing – review & editing, Supervision, Resources, Investigation. **Joaquim L. Faria:** Writing – review & editing, Investigation, Funding acquisition. **Maria J. Sampaio:** Writing – review & editing, Visualization, Validation, Supervision, Methodology, Investigation, Formal analysis, Conceptualization.

Declaration of competing interest

The authors declare that they have no known competing financial interests or personal relationships that could have appeared to influence the work reported in this paper.

Acknowledgments

This work was supported by national funds through FCT/MCTES (PIDDAC): LSRE-LCM, UIDB/50020/2020 (DOI: 10.54499/UIDB/50020/2020) and UIDP/50020/2020 (DOI: 10.54499/UIDP/50020/2020); and ALiCE, LA/P/0045/2020 (DOI: 10.54499/LA/P/0045/2020). M.J.S. acknowledges FCT funding under the Scientific Employment Stimulus - Institutional Call (CEECINST/00010/2021/CP1770/CT0011). A.L.M. thanks her scholarship to the Fundação Calouste Gulbenkian. JCL acknowledges the PhD research grant from FCT, Ref. 2020.04651.BD (DOI: 10.54499/2020.04651.BD).

Supplementary materials

Supplementary material associated with this article can be found, in the online version, at doi:10.1016/j.ceja.2024.100697.

Data availability

Data will be made available on request.

References

[1] C. Tarhan, M.A. Çil, A study on hydrogen, the clean energy of the future: hydrogen storage methods, J. Energy Storage 40 (2021) 102676, https://doi.org/10.1016/j.est.2021.102676.

[2] A.F. Alkaim, T.A. Kandiel, R. Dillert, D.W. Bahnemann, Photocatalytic hydrogen production from biomass-derived compounds: a case study of citric acid, Environ. Technol. (Singap. World Sci.) (United Kingdom) 37 (21) (2016) 2687–2693, https://doi.org/10.1080/09593330.2016.1158871.

[3] D.V. Esposito, R.V. Forest, Y. Chang, N. Gaillard, B.E. McCandless, S. Hou, K.H. Lee, R.W. Birkmire, J.G. Chen, Photoelectrochemical reforming of glucose for hydrogen production using a WO3-based tandem cell device, Energy Environ. Sci. 5 (10) (2012) 9091–9099, https://doi.org/10.1039/c2ee22560c.

[4] Q. Yang, T. Wang, F. Han, Z. Zheng, B. Xing, B. Li, Bimetal-modified g-C3N4 photocatalyst for promoting hydrogen production coupled with selective oxidation of biomass derivative, J. Alloys Compd. 897 (2022), https://doi.org/10.1016/j.jallcom.2021.163177.

[5] D. Zhou, D. Li, S. Yuan, Z. Chen, Recent advances in biomass-based photocatalytic H_2 production and efficient photocatalysts: a review, Energy Fuels 36 (18) (2022) 10721–10731, https://doi.org/10.1021/acs.energyfuels.2c01904.

[6] N. Naffati, M.J. Sampaio, E.S. Da Silva, M.F. Nsib, Y. Arfaoui, A. Houas, J.L. Faria, C.G. Silva, Carbon-nanotube/TiO_2 materials synthesized by a one-pot oxidation/hydrothermal route for the photocatalytic production of hydrogen from biomass derivatives, Materials (Basel)Mater. Sci. Semicond. Process. 115 (2020), https://doi.org/10.1016/j.mssp.2020.105098.

[7] C.G. Silva, M.J. Sampaio, R.R.N. Marques, L.A. Ferreira, P.B. Tavares, A.M.T. Silva, J.L. Faria, Photocatalytic production of hydrogen from methanol and saccharides using carbon nanotube-TiO_2 catalysts, Appl. Catal. B: Environ. 178 (2015) 82–90, https://doi.org/10.1016/j.apcatb.2014.10.032.

[8] M. Singh, D.C. Cha, H. Kim, J. Park, S. Kim, C.G. Yoo, G. Leem, S. Lee, Photocatalysis-Derived Biomass Conversion For Green Hydrogen Production, Towards Sustainable and Green Hydrogen Production by Photocatalysis: Insights into Design and Development of Efficient Materials (Volume 2), American Chemical Society, 2024, pp. 47–78, https://doi.org/10.1021/bk-2024-1468.ch003.

[9] S. Dhingra, M. Sharma, V. Krishnan, C.M. Nagaraja, Design of noble metal-free CoTiO3/Zn0.5Cd0.5S heterostructure photocatalyst for selective synthesis of furfuraldehyde combined with H_2 production, J. Colloid Interface Sci. 608 (2022) 1040–1050, https://doi.org/10.1016/j.jcis.2021.10.031.

[10] W. Li, X.-s. Chu, F. Wang, Y.-y. Dang, X.-y. Liu, X.-c. Wang, C.-y. Wang, Enhanced cocatalyst-support interaction and promoted electron transfer of 3D porous g-C_3N_4/GO-M (Au, Pd, Pt) composite catalysts for hydrogen evolution, Appl. Catal. B Environ. 288 (2021) 120034, https://doi.org/10.1016/j.apcatb.2021.120034.

[11] W. Li, X. Wang, M. Li, S.-a. He, Q. Ma, X. Wang, Construction of Z-scheme and p-n heterostructure: three-dimensional porous g-C_3N_4/graphene oxide-Ag/AgBr composite for high-efficient hydrogen evolution, Appl. Catal. B Environ. 268 (2020) 118384, https://doi.org/10.1016/j.apcatb.2019.118384.

[12] Q. Liu, W. Luan, X. Zhang, R. Zhao, J. Han, L. Wang, $NiMoP_2$ co-catalyst modified Cu doped ZnS for enhanced photocatalytic hydrogen evolution, Sep. Purif. Technol. 354 (2025) 128666, https://doi.org/10.1016/j.seppur.2024.128666.

[13] X. Liu, M. Dou, G. Yang, E. Liu, Z. Li, B. Han, H. Yang, D. Li, J. Dou, Modulation of catalyst interfacial electric field and charge transfer promotes NiS-modified $CoWO_4$/$ZnIn_2S_4$ S-scheme heterojunction for efficient photocatalytic hydrogen evolution, Sep. Purif. Technol. 354 (2025) 128680, https://doi.org/10.1016/j.seppur.2024.128680.

[14] A. Speltini, F. Gualco, F. Maraschi, M. Sturini, D. Dondi, L. Malavasi, A. Profumo, Photocatalytic hydrogen evolution assisted by aqueous (waste)biomass under simulated solar light: oxidized g-C_3N_4 vs. P25 titanium dioxide, Int. J Hydrogen Energy 44 (8) (2019) 4072–4078, https://doi.org/10.1016/j.ijhydene.2018.12.126.

[15] V.N. Rao, T.J. Malu, K.K. Cheralathan, M. Sakar, C.M. Hussain, M.M. Kumari, M. V. Shankar, Emerging trends in photocatalytic transformation of biomass-derived glycerol into hydrogen fuel and value-added chemicals. Handbook of Smart Photocatalytic Materials: Environment, Energy, Emerging Applications and Sustainability, 2020, pp. 227–246, https://doi.org/10.1016/B978-0-12-819049-4.00017-9.

[16] A. Puga, Photocatalytic hydrogen production in the context of sustainable energy, Photocat. Hydrogen Prod. Sustain. Energy (2023) 1–18, https://doi.org/10.1002/9783527835423.ch1.

[17] D. Ouyang, F. Wang, D. Gao, W. Han, X. Hu, D. Qiao, X. Zhao, Light-driven lignocellulosic biomass conversion for production of energy and chemicals, iScience 25 (10) (2022), https://doi.org/10.1016/j.isci.2022.105221.

[18] Y. Meng, Y. Jian, J. Li, H. Wu, H. Zhang, S. Saravanamurugan, S. Yang, H. Li, Surface-active site engineering: synergy of photo- and supermolecular catalysis in hydrogen transfer enables biomass upgrading and H2 evolution, Chem. Eng. J. 452 (2023), https://doi.org/10.1016/j.cej.2022.139477.

[19] S. Dhingra, M. Sharma, V. Krishnan, C.M. Nagaraja, Design of noble metal-free NiTiO3/ZnIn2S4 heterojunction photocatalyst for efficient visible-light-assisted production of H2 and selective synthesis of 2,5-Bis(hydroxymethyl)furan, J. Colloid Interface Sci. 615 (2022) 346–356, https://doi.org/10.1016/j.jcis.2022.01.190.

[20] X. Hu, Z. Zhan, J. Zhang, I. Hussain, B. Tan, Immobilized covalent triazine frameworks films as effective photocatalysts for hydrogen evolution reaction, Nat. Commun. 12 (1) (2021) 6596, https://doi.org/10.1038/s41467-021-26817-4.

[21] R.A. Borges, M.F. Pedrosa, Y.A. Manrique, C.G. Silva, A.M.T. Silva, J.L. Faria, M. J. Sampaio, 3D structured photocatalysts for sustainable H_2O_2 generation from saccharides derivatives, Chem. Eng. J. 470 (2023) 144066, https://doi.org/10.1016/j.cej.2023.144066.

[22] M.J. Sampaio, A.R.L. Ribeiro, C.M.R. Ribeiro, R.A. Borges, M.F. Pedrosa, A.M. T. Silva, C.G. Silva, J.L. Faria, A technological approach using a metal-free immobilized photocatalyst for the removal of pharmaceutical substances from urban wastewaters, Chem. Eng. J. 459 (2023) 141617, https://doi.org/10.1016/j.cej.2023.141617.

[23] F. Dong, Z. Wang, Y. Li, W.-K. Ho, S.C. Lee, Immobilization of polymeric g-C3N4 on structured ceramic foam for efficient visible light photocatalytic air purification with real indoor illumination, Environ. Sci. Technol. 48 (17) (2014) 10345–10353, https://doi.org/10.1021/es502290f.

[24] A.Y. Shan, T.I.M. Ghazi, S.A. Rashid, Immobilisation of titanium dioxide onto supporting materials in heterogeneous photocatalysis: a review, Appl. Catal. A Gen. 389 (1) (2010) 1–8, https://doi.org/10.1016/j.apcata.2010.08.053.

[25] J.C. Lopes, M.J. Sampaio, B. Rosa, M.J. Lima, J.L. Faria, C.G. Silva, Role of TiO2-based photocatalysts on the synthesis of the pharmaceutical precursor benzhydrol by UVA-LED radiation, J. Photochem. Photobiol. A: Chem. (Easton) 391 (2020) 112350, https://doi.org/10.1016/j.jphotochem.2019.112350.

[26] F. Liu, N.A. Hashim, Y. Liu, M.R.M. Abed, K. Li, Progress in the production and modification of PVDF membranes, J. Memb. Sci 375 (1) (2011) 1–27, https://doi.org/10.1016/j.memsci.2011.03.014.

[27] M. Peñas-Garzón, M.J. Sampaio, Y.L. Wang, J. Bedia, J.J. Rodriguez, C. Belver, C. G. Silva, J.L. Faria, Solar photocatalytic degradation of parabens using UiO-66-NH_2, Sep. Purif. Technol. 286 (2022) 120467, https://doi.org/10.1016/j.seppur.2022.120467.

[28] X. Gao, X. Liu, Z. Zhu, X. Wang, Z. Xie, Enhanced photoelectrochemical and photocatalytic behaviors of MFe2O4 (M = Ni, Co, Zn and Sr) modified TiO_2 nanorod arrays, Sci. Rep. 6 (1) (2016) 30543, https://doi.org/10.1038/srep30543.

[29] S.A. Althabaiti, Z. Khan, M.A. Malik, S.M. Bawaked, S.Z. Al-Sheheri, M. Mokhtar, S. I. Siddiqui, K. Narasimharao, Biomass-derived carbon deposited TiO_2 nanotube photocatalysts for enhanced hydrogen production, Nanoscale Adv. 5 (14) (2023) 3671–3683, https://doi.org/10.1039/D3NA00211J.

[30] R.K. Srivastava, N.P. Shetti, K.R. Reddy, E.E. Kwon, M.N. Nadagouda, T. M. Aminabhavi, Biomass utilization and production of biofuels from carbon neutral materials, Environ. Pollut. 276 (2021) 116731, https://doi.org/10.1016/j.envpol.2021.116731.

[31] M. Harada, H. Einaga, Formation mechanism of Pt particles by photoreduction of Pt ions in polymer solutions, Langmuir. 22 (5) (2006) 2371–2377, https://doi.org/10.1021/la052378m.

[32] Y.-H. Yao, Y. Yang, Y. Wang, H. Zhang, H.-L. Tang, H.-Y. Zhang, G. Zhang, Y. Wang, F.-M. Zhang, H. Yan, Photo-induced synthesis of ternary Pt/rGO/COF photocatalyst with Pt nanoparticles precisely anchored on rGO for efficient visible-light-driven H2 evolution, J. Colloid Interface Sci. 608 (2022) 2613–2622, https://doi.org/10.1016/j.jcis.2021.10.183.

[33] J. Zhang, L. Zheng, F. Wang, C. Chen, H. Wu, S.A.K. Leghari, M. Long, The critical role of furfural alcohol in photocatalytic H_2O_2 production on TiO_2, Appl. Catal. B Environ. 269 (2020) 118770, https://doi.org/10.1016/j.apcatb.2020.118770.

[34] I.A. Shkrob, M.C. Sauer, D. Gosztola, Efficient, rapid photooxidation of chemisorbed polyhydroxyl alcohols and carbohydrates by TiO_2 nanoparticles in an

aqueous solution, J. Phys. Chem. (Easton) B 108 (33) (2004) 12512–12517, https://doi.org/10.1021/jp0477351.
[35] V.-H. Dang, T.-A. Nguyen, M.-V. Le, D.Q. Nguyen, Y.H. Wang, J.C.S. Wu, Photocatalytic hydrogen production from seawater splitting: current status, challenges, strategies and prospective applications, Chem. Eng. J. 484 (2024) 149213, https://doi.org/10.1016/j.cej.2024.149213.
[36] Y. Wang, J. Zhou, F. Wang, Y. Xie, S. Liu, Z. Ao, C. Li, Hydrogen generation from photocatalytic treatment of wastewater containing pharmaceuticals and personal care products by Oxygen-doped crystalline carbon nitride, Sep. Purif. Technol. 296 (2022) 121425, https://doi.org/10.1016/j.seppur.2022.121425.
[37] M.S. Yesupatham, A. Augustin, N. Agamendran, B. Honnappa, M. Shanmugam, P.J. J. Sagayaraj, G. Thennarasu, N.C. Sagaya Selvam, K. Sekar, Photocatalytic seawater splitting for hydrogen fuel production: impact of seawater components and accelerating reagents on the overall performance, Sustain. Energy Fuels. 7 (19) (2023) 4727–4757, https://doi.org/10.1039/D3SE00810J.
[38] M. Gryta, Long-term performance of membrane distillation process, J. Memb. Sci. 265 (1) (2005) 153–159, https://doi.org/10.1016/j.memsci.2005.04.049.